Weak localization in electric-double-layer gated few-layer graphene

2D Materials

OPEN ACCESS

PAPER

Weak localization in electric-double-layer gated few-layer graphene

R S Gonnelli[1], E Piatti[1], A Sola[1,5], M Tortello[1], F Dolcini[1,2], S Galasso[1], J R Nair[1], C Gerbaldi[1], E Cappelluti[3], M Bruna[4] and A C Ferrari[4]

[1] Dipartimento di Scienza Applicata e Tecnologia, Politecnico di Torino, 10129 Torino, Italy
[2] Istituto CNR-SPIN, Monte S.Angelo—via Cinthia, I-80126 Napoli, Italy
[3] Istituto dei Sistemi Complessi del CNR, 00185 Roma, Italy
[4] Cambridge Graphene Centre, University of Cambridge, Cambridge, CB3 OFA United Kingdom
[5] Present address: Istituto Nazionale di Ricerca Metrologica (INRIM), 10135 Torino, Italy

E-mail: renato.gonnelli@polito.it

RECEIVED
28 October 2016

REVISED
22 December 2016

ACCEPTED FOR PUBLICATION
16 January 2017

PUBLISHED
7 July 2017

Keywords: few-layer graphene, EDL gating, liquid gating, weak localization, quantum transport, scattering lifetimes

Abstract

We induce surface carrier densities up to $\sim 7 \cdot 10^{14}$ cm^{-2} in few-layer graphene devices by electric double layer gating with a polymeric electrolyte. In 3-, 4- and 5-layer graphene below 20–30 K we observe a logarithmic upturn of resistance that we attribute to weak localization in the diffusive regime. By studying this effect as a function of carrier density and with *ab initio* calculations we derive the dependence of transport, intervalley and phase coherence scattering lifetimes on total carrier density. We find that electron–electron scattering in the Nyquist regime is the main source of dephasing at temperatures lower than 30 K in the $\sim 10^{13}$ cm^{-2} to $\sim 7 \cdot 10^{14}$ cm^{-2} range of carrier densities. With the increase of gate voltage, transport elastic scattering is dominated by the competing effects due to the increase in both carrier density and charged scattering centers at the surface. We also tune our devices into a crossover regime between weak and strong localization, indicating that simultaneous tunability of both carrier and defect density at the surface of electric double layer gated materials is possible.

1. Introduction

Electrolytic gating, initially developed for polymeric transistors (see ref. [1] and references therein), is now used to study the transport properties of a wide range of materials, from semiconductors [2], to insulators [3] and superconductors [4–6]. This technique induces an orders-of-magnitude enhancement in the electric field at the sample surface, when compared to conventional solid gate techniques [7–10]. When a potential is applied between the sample and a counter electrode, the ions inside the polymeric (or liquid) electrolyte migrate and accumulate at the two surfaces, building up the so-called electric double layer (EDL) [7, 8]. This acts as a nanoscale capacitor, and allows one to obtain surface variations of the carrier density, n_{2d}, up to $\sim 10^{14}$–10^{15} cm^{-2} [5], depending on the density of states of the sample and the electrochemical stability window of the electrolyte itself.

We firstly exploited an EDL to gate single layer graphene (SLG) in ref. [11] and bilayer graphene (BLG) in ref. [12]. Since then, this technique has been widely applied to study the transport properties of SLG [13–15] and few-layer graphene (FLG) [16–18]. Refs. [14, 15] studied the dominant scattering mechanisms in SLG for n_{2d} up to 6 and $11 \cdot 10^{13}$ cm^{-2}, respectively. Ref. [15] reported a gate-tunable crossover of the resistivity from $\rho \propto T$ to $\rho \propto T^4$, in the range from 1.5 K up to room temperature (RT). This provides a clear example of Bloch–Grüneisen behavior in two dimensions (2d) due to a crossover from small-angle to large-angle electron–phonon (e–ph) scattering [19]. Ref. [16] reported an electric field-induced, gate-tunable band gap in rhombohedral stacked three-layer graphene (3LG) for $n_{2d} \lesssim 1 \cdot 10^{13}$ cm^{-2}. Ref. [17] showed that the n_{2d} achievable by electrolyte gating is large enough to populate the higher-energy bands in two layer (2LG) and three layer (3LG) graphene, away from the charge neutrality point. Ref. [18] demonstrated a gate-tunable crossover from weak localization (WL) to weak anti-localization (WAL) in the low-T transport properties of 3LG on SiC.

We reported n_{2d} up to ~ 3.5–$4.5 \cdot 10^{15}$ cm^{-2} in thin films of Au and other noble metals with EDL gating by using a polymer electrolyte system (PES) of improved capacitance [21, 22] compared to previous experiments [7–10]. By using the same PES, we induced $n_{2d} > 6 \cdot 10^{14}$ cm^{-2} in few-layer graphene (FLG)

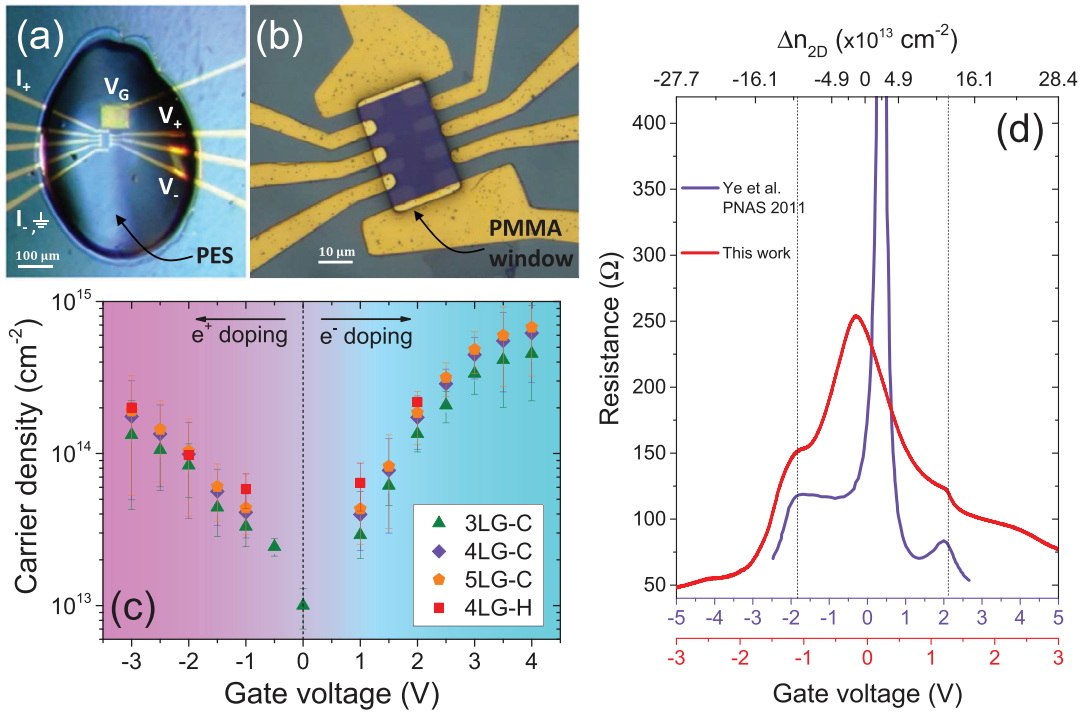

Figure 1. (a) FLG device covered by drop-cast PES; (b) Zoom in the region of the Hall-bar shaped FLG channel of a second device showing the PMMA window, and the current and voltage contacts; (c) n_{2d} as a function of V_G. In the legend, C stands for 'determined by double-step chronocoulometry', while H means 'determined by Hall-effect measurements'; (d) Resistance curve as a function of V_G and of the induced carrier density $\Delta n_{2d} = n_{2d}(V_G) - n_{2d}(0)$ of one of our 3LG devices, compared with ref. [17].

mechanically exfoliated from highly oriented pyrolytic graphite (HOPG) [23]. One of the challenges at such high n_{2d} is the observation of quantum phenomena, such as superconductivity. The induction of superconducting order in graphene would greatly benefit the development of novel device concepts [24], such as atomic-scale superconducting transistors [25], and superconductor-quantum dot devices [26, 27]. Superconductivity was reported in EDL gated MoS_2 [6] and WS_2 [20]. Refs. [24, 28] theoretically predicted that this should also be the case for graphene. However, the experimental search for superconductivity in graphene via EDL-gating has so far been unsuccessful [15, 23], while low-T superconductivity has been demonstrated by alkali-metal decoration [29] and intercalation [30].

Here, we focus on the transport properties of EDL-gated 3LG, four (4LG) and five layer graphene (5LG) in the 4–30 K range. We find a small ($\lesssim$1.5%), gate tunable, upturn in the sheet resistance, R_S, below ~20–30 K. This shows a logarithmic T dependence, and its intensity is inversely correlated with n_{2d}. We demonstrate by magnetoresistance measurements that WL in the diffusive regime is at the origin of the upturn. This agrees well with the theoretical models developed for SLG and 2LG. Combining experiments with *ab initio* calculations we extract the dependence of the characteristic scattering lifetimes with both T and n_{2d}. From the dephasing lifetime dependence on T, we find that the dominant inelastic scattering mechanism for $T \lesssim 20$ K is electron–electron (e–e) scattering with small momentum transfer (Nyquist term) [55]. From its dependence on n_{2d}, we show that EDL gating brings the system in a crossover condition from WL to strong localization, and that this is gate-tunable in 5LG. Our results demonstrate quantum coherent transport in 4LG and 5LG for carrier densities in excess of $\sim 10^{13}$–10^{14} cm^{-2}.

2. Fabrication and characterization

FLG flakes are prepared by micromechanical exfoliation of graphite on Si/SiO_2 [32, 33]. The number of layers, N, is determined by a combination of Raman spectroscopy [34, 35] and optical microscopy [31, 36]. EDL field-effect devices are then prepared by electron beam lithography and deposition of Cr/Au contacts in the Hall bar configuration, as shown in figure 1(b). A coplanar gate contact is deposited on the side. A protective poly(methyl methacrylate) (PMMA) layer is spin-coated, patterned and hard-baked on the completed devices in order to avoid interactions between the electrolyte and the metallic leads. A reactive mixture precursor of the PES is then drop-cast onto the whole device and UV-cured, to get a cross-linked photopolymer electrolyte [21, 23], figure 1(a). The precursor viscous liquid reactive mixture is composed of methacrylic oligomers and lithium salt: bisphenol A ethoxylate dimethacrylate (BEMA; average Mn: 1700, Aldrich), poly(ethylene glycol)methyl ether methacrylate (PEGMA; average Mn: 475, Aldrich), and 10% of lithium bis(trifluoromethanesulfonyl)

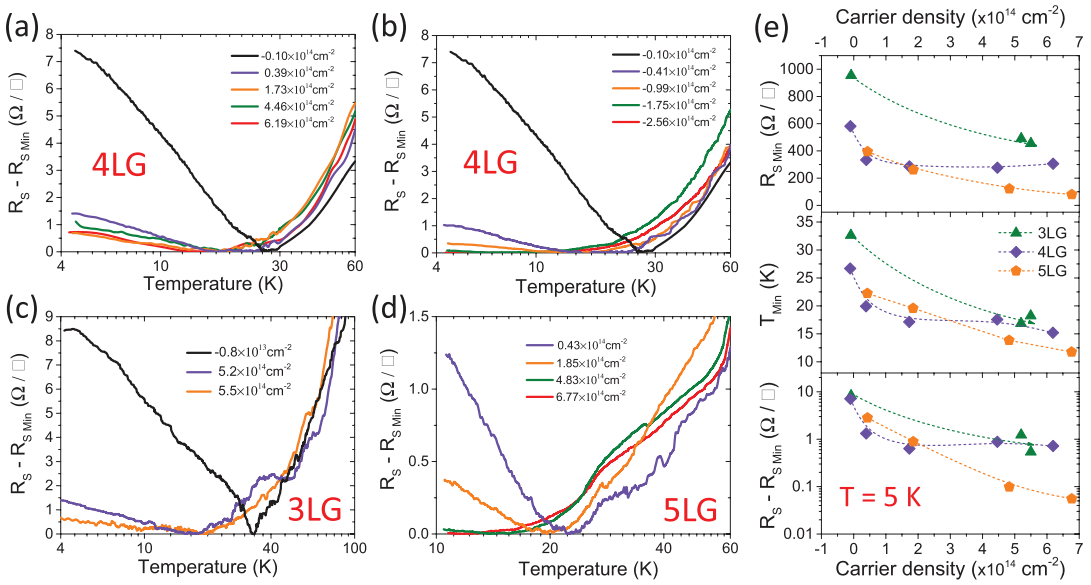

Figure 2. Semi-logarithmic plot of the increase of R_S with respect to its minimum R_{SMin} as a function of T in (a) 4LG for different values of electron doping; (b) the same device for different values of hole doping; (c) 3LG and (d) 5LG for different values of electron doping. Solid black curves refer to the transport data measured at $V_G = 0$ and are reported in all panels as a reference. In panel (d), the $V_G = 0$ curve is not reported since 5LG does not show a metallic behavior at $V_G = 0$ [23]; (e) Carrier density dependencies of R_{SMin} (top panel), temperature where the minimum is reached (T_{Min}, central panel), and R_S increase at $T = 5$ K (bottom panel), for different N. Dashed lines are guides to the eye.

imide (LiTFSI) along with the addition of 3 wt% 2-hydroxy-2-methyl-1-phenyl-1-propanon as the free radical photoinitiator (Darocur 1173, Ciba Specialty Chemicals). No annealing is performed in the time between contact deposition and PES casting, and the devices are stored in a desiccator under low vacuum ($\sim 10^{-1}$–1 mbar) to prevent contamination. We do not perform any annealing step before double-step chronocoulometry and transport measurements, because we are not interested in probing the properties of our samples close to the Dirac point. Thus, n_{2d} near the charge neutrality point is larger compared to the typical values for exfoliated flakes ($\sim 10^{11}$–10^{12} cm^{-2}) [66, 67]. Four-wire resistance measurements are done under high vacuum ($<10^{-5}$ mbar) in the chamber of a Cryomech pulse-tube cryocooler via a Keithley 6221/2182A current source/nanovoltmeter assembly. The gate potential is controlled through a Keithley 2410 sourcemeter, whose negative electrode is set at the current drain contact. Gate leakage is monitored to ensure that no electrochemical reactions occur at the graphene/EDL interface. Magnetoresistance measurements are performed in an Oxford Instruments helium cryostat equipped with a superconducting magnet.

We estimate n_{2d} as a function of the gate voltage, V_G, from the measured gate current through double-step chronocoulometry [39] (DSCC), as shown in figure 1(c) for 3LG, 4LG and 5LG (green triangles, violet diamonds and orange pentagons, respectively) and described in detail in ref. [23]. This technique is based on the fact that, in absence of chemical reactions at the electrodes, the current flowing through the electrolyte can be split into two contributions [39]. The first, due to the EDL build-up, decays exponentially over time [39]. The second, due to ion diffusion through the bulk of the electrolyte [39], decays as the square root of time [39]. By fitting the gate current response to a step-like application and removal of V_G with a function that separately accounts for both effects, the two contributions can be distinguished and, thus, the EDL charge estimated. Further details on the technique can be found in refs. [21, 23, 39]. These results are checked with independent Hall-effect measurements performed on a 4LG device (red squares in figure 1(c)). We conservatively use the DSCC values in the full V_G range.

We also compare the RT resistance as a function of V_G in a 3LG with the earlier measurements of ref. [17]. Figure 1(d) shows how, in both cases, regions of sharp non-monotonic behavior are present in the resistance curves away from the Dirac point. The position of these upturns is associated with a specific charge density, such that the Fermi level, E_F, is crossing the bottom of the split-off bands [17], which can be used for voltage-n_{2d} calibration. This comparison indicates that our PES allows us to reach the split-off bands at lower potential than the ionic liquid of ref. [17], thus supporting a higher charge induction capability.

3. Results and discussion

We first measure the four-contact resistance in the 4–290 K range as a function of N and n_{2d}. In each measurement, V_G is applied at RT and the system

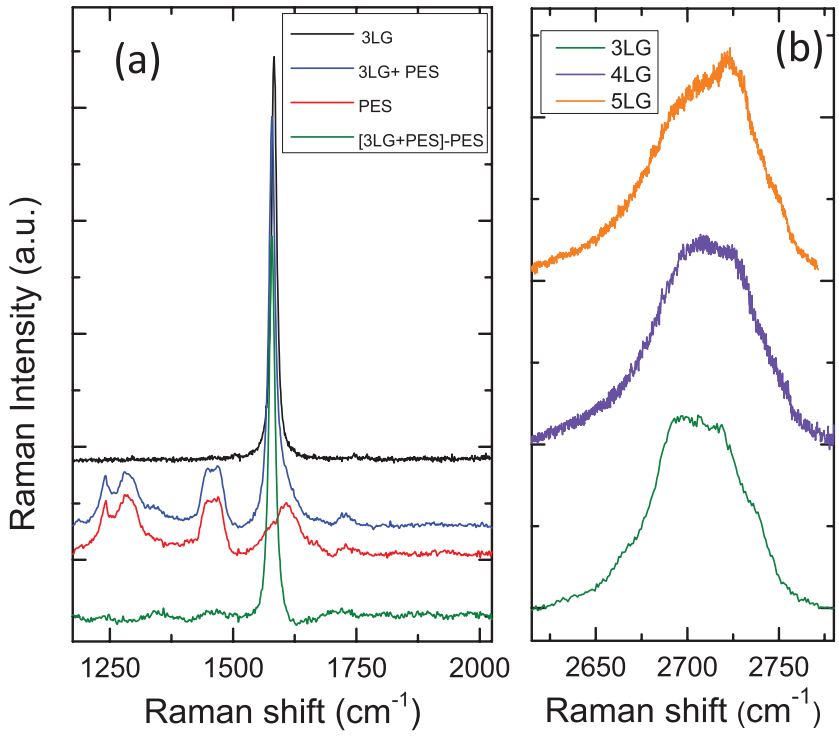

Figure 3. (a) Raman spectrum measured at 514 nm for a 3LG device, before (black) and after (blue) PES drop-casting, together with the Raman response from the PES (red) and the spectrum with the subtracted background (green). (b) Raman 2D region for 3LG (green), 4LG (violet) and 5LG (orange).

is then cooled to a base $T \sim 4$–10 K, depending on sample. Any further modification of n_{2d} below the PES glass transition at ∼230 K [23] is prevented by the quenched ion motion [4, 6]. The samples are then allowed to spontaneously warm up, taking advantage of the absence of T fluctuations associated with the cryocooler's thermal cycles. We reported a detailed analysis of the T dependence of R_S for these device in the 30–290 K range in ref. [23]. Here we focus on the anomalous behavior that emerges in the 4–30 K range.

For all the three N, a logarithmic upturn is observed for $T \lesssim 30$ K in the resistance curves for samples in the metallic regime, as shown in figure 2. Figures 2(a)–(d) plot the low-T ($\lesssim$100 K) variations of R_S with respect to its minimum value R_{SMin} for 3LG, 4LG and 5LG as function of T in a semi-logarithmic scale. R_{SMin} decreases with increasing n_{2d} for all N, and saturates for 4LG (see top panel of figure 2(e)). Both the amplitude of the logarithmic upturn ($R_S(5K) - R_{SMin}$) and the T_{Min} at which R_{SMin} is reached strongly depend on n_{2d} and N, as shown in the central and bottom panels of figure 2(e). Similar logarithmic upturns in the resistance of conductors in the diffusive regime, such as Si MOSFETs [41], GaAs heterostructures [42,43], and transition metal alloys [44] are usually attributed to Kondo effect [45], WL [46,47], and e−e interactions [50–52], or to a superposition of any of the previous sources [49].

We first consider the Kondo effect, which is caused by carrier scattering from diluted magnetic impurities [44, 45]. Unlike in ref. [48], we do not intentionally introduce any defects in our samples. We thus employ Raman spectroscopy to monitor the amount of Raman active defects in our devices, before and after PES drop-casting. Raman measurements are carried out at RT in a Renishaw InVia microspectrometer equipped with a 100X objective. The spot size is ∼1 μm, the excitation wavelength is 514 nm and the incident power is kept well below 1 mW in order to avoid heating. Figure 3(a) plots the Raman spectrum of a 3LG device. The PES shows several peaks between ∼1000 and 1500 cm^{-1}. The broad peak between ∼1400 and 1500 cm^{-1} can be assigned to the methylene bending mode [102], the peak at ∼1280 cm^{-1} to methylene twisting [103], and that at ∼1243 cm^{-1} to either trifluoromethyl stretching [102] or methylene twisting [103].

We perform a background subtraction by normalizing to the low-frequency PES peaks near the D peak. This gives an upper limit for the ratio between the intensity of the D peak and the intensity of the G peak, I(D)/I(G), ∼0.015, which leads to an estimated defect density $\sim 3 \cdot 10^9$ cm^{-2} [37, 38]. For comparison, in order to obtain a sizeable Kondo effect ($\delta\rho/\rho \simeq 6\%$ at $T = 0.3$ K), in ref. [48] it was necessary to induce a defect density $\sim 3 \cdot 10^{11}$ cm^{-2}, which produced a corresponding I(D)/I(G) ∼2.8, for an excitation wavelength of 633 nm [48]. Our values indicate that our devices are at least two orders of magnitude less defective. Thus, we discard contributions from the Kondo effect to the resistance upturn.

3.1. Weak localization in few-layer Graphene

WL arises from the constructive interference between pairs of time-reversed trajectories of electrons

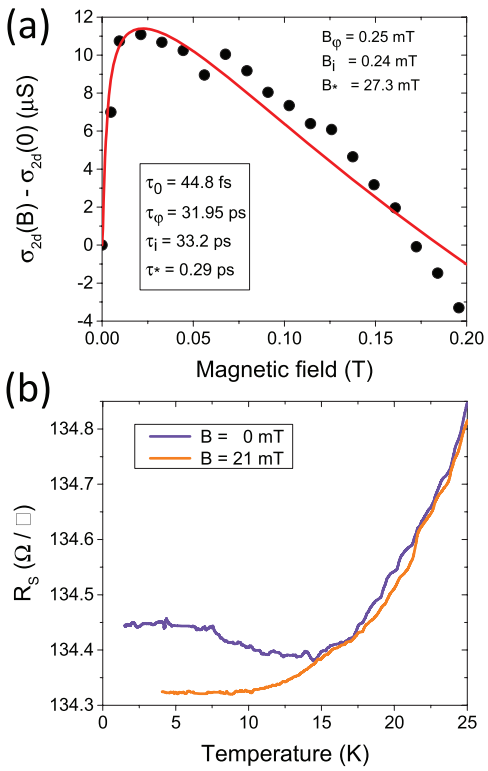

Figure 4. (a) B dependence of conductance relative to the value at zero field (black circles) and fit by using equation (2) (red solid line) for 3LG. (b) R_S as a function of T for the 3LG device of figure 4(a) for $B = 0.021$ T and 0T.

elastically scattering in a closed loop [49]. This increases the probability of charge-carrier backscattering in a conductor in the diffusive regime [46, 47], thus reducing the conductance [49]. In order for WL to appear, phase coherence must be maintained throughout the entire closed loop, followed by the electrons undergoing elastic scattering, as described by a characteristic lifetime τ_e [46]. WL is thus suppressed by an increased probability of inelastic scattering associated with the T increase [46]. The average time interval in which phase coherence is maintained is called phase coherence lifetime τ_φ [49]. Typically, two inelastic processes determine τ_φ [49]. E–ph scattering [53], which is important for higher T [49], and e–e scattering [54, 55], which dominates for lower T [49]. The T that marks a crossover between these two scattering processes depends on the transport properties of each material [49], and it is typically of the order of few tens K [49].

In a diffusive system a conductivity suppression at low T may also be caused by e–e interactions, as a result of the diffraction of an electron wave by the oscillations in the electrostatic potential generated by the other electrons [49–52]. A widely exploited approach to discriminate between these two contributions is the measurement of the sample magnetoconductance [49, 50, 56]. In the presence of a perpendicular magnetic field B, time-reversal symmetry is broken [49]. A phase difference arises between any two time-reversed electron trajectories, whose constructive interference, in principle able to localize electrons [49], is therefore broken [56]. As a consequence [49]: (i) a negative magnetoconductance is associated with WAL [57]; (ii) a vanishing magnetoconductance is associated with e–e interaction (insensitive to B) [56]; (iii) a positive magnetoconductance is associated with WL [56, 57].

In order to determine the origin of the resistance upturn we thus measure the magnetoconductance of a 3LG device at 2 K. We find it positive, and reaching a maximum at $B_\varphi = 2\hbar/4ev_F^2\tau_e\tau_\varphi = 0.021$ T, as shown in figure 4(a), where the magnetoconductance relative to the value at zero field is plotted as a function of B. In order to rule out even a partial contribution from e–e interactions, we also measure the device resistance while heating the sample under $B = B_\varphi$. Figure 4(b) shows that the logarithmic upturn is suppressed within the noise level. This behavior is reversible upon removal of B. The logarithmic upturn saturates for $T \lesssim 4$ K, a feature usually assigned to the effect of finite channel size [66]. These data support the conclusion that, in our devices, WL is the source of the measured resistance upturn and that the logarithmic correction to the conductivity due to e–e interaction can be disregarded. This is in contrast with earlier reports on SLG, where both contributions were shown to be relevant [69]. We also note that the magnetoconductance behavior of our 3LG is qualitatively different from that in ref. [18], where spin–orbit coupling was found to affect the magnetoconductance behavior of EDL-gated 3LG. We do not observe any significant influence of spin–orbit coupling. We note, however, that the devices reported in ref. [18] were obtained from FLG grown on silicon carbide. The enhanced spin–orbit coupling reported in ref. [18] may thus be associated both with the different fabrication process and substrate.

The carrier lifetimes determine the WL behavior [49, 57], and can thus be obtained from figure 4(a) [58, 59]. In SLG it was predicted that, due to lattice symmetries, an additional π Berry phase is accumulated by charge carriers scattering in closed loops [62–64]. In 2LG such additional Berry phase is instead 2π [59, 65]. This means that in SLG the quantum interference due to localization is always destructive [60, 61], leading to an anti-localization [57], while in 2LG the effect of the additional phase cancels out, and the material should retain the standard WL behavior [59]. In addition, WAL, where the underlying elastic scattering mechanism is due to charged impurities, is strongly suppressed by intervalley scattering and trigonal warping [58]. Furthermore, refs. [58, 59] showed that SLG and 2LG have another quantum correction to the Drude resistivity, always localized, due to elastic intervalley scattering, and not affected by trigonal warping. As a consequence, various localization behaviors were reported [57, 66, 67, 81–85], depending on the sample preparation and on the explored regime.

To the best of our knowledge, a WL model for $N > 2$ has not yet been developed. Earlier WL reports in FLG made use of models developed for SLG and 2LG [89–91].

The simultaneous presence of both Dirac-like and parabolic bands in odd-N flakes [92, 93] makes an *a priori* determination of the total Berry phase difficult. The correction to the conductance due to the Berry phase is suppressed in all our experiments. This allows us to conclude that only elastic intervalley scattering is relevant for quantum interference.

Following the theoretical approach of ref. [59], the T dependence of the quantum correction to the 2d conductance is determined by the T behavior of the phase coherence lifetime τ_φ, as:

$$\delta\sigma_{\rm WL}(T) = -\frac{e^2}{\pi h}\ln\left[1+2\frac{\tau_\varphi(T)}{\tau_i}\right] - \delta_0(\tau_\varphi, \tau_{\rm tr}, \tau_*) \quad (1)$$

where τ_i is the intervalley scattering lifetime, $\tau_{\rm tr} = 2\tau_e$ is the transport lifetime (associated with scattering from charged impurities [66, 67]) and τ_* is an effective lifetime associated with intravalley scattering and trigonal warping. On the right hand side of equation (1), the first term arises from intervalley scattering, and resembles the conventional WL correction [49], apart from the factor two and the different elastic lifetime involved. Since the argument of the logarithm is always greater than one, this term is always negative. The second term, arising from intravalley scattering, is positive or negative depending on the Berry phase, and is strongly suppressed the larger the value of τ_*^{-1} [58, 59]. The B dependence of the quantum correction to the conductance can be written as [58, 59]:

$$\delta\sigma_{\rm WL}({\rm B}) = \frac{e^2}{\pi h}\left[F\left(\frac{\rm B}{{\rm B}_\varphi}\right) - F\left(\frac{\rm B}{{\rm B}_\varphi + 2B_i}\right)\right] + \delta({\rm B}, {\rm B}_\varphi, B_*) \quad (2)$$

where:

$$F(z) = \ln(z) + \psi(1/2 + 1/z)$$

and

$$B_{\varphi,i,*} = (\hbar/4D_{\rm tr}e)\tau^{-1}_{\varphi,i,*}$$

with ψ denoting the digamma function [59], $D_{\rm tr} = v_{\rm F}^2\tau_{\rm tr}$ the diffusion coefficient [59], and $v_{\rm F}$ the Fermi velocity. We obtain $\tau_{\rm tr}$ by combining the measurement of $R_{\rm SMin}$ with *ab initio* DFT calculations (see equation (7)). This gives $\tau_{\rm tr} = 44.8$ fs and $D_{\rm tr} = 448$ cm^2 s^{-1} used henceforth.

For the data in figure 4(a) (3LG), the Berry phase is π and $\delta({\rm B}, {\rm B}_\varphi, {\rm B}_*) = -(4e^2/\pi h)F({\rm B}/({\rm B}_\varphi + {\rm B}_*))$. We therefore use equation (2) to fit σ_{2d} as a function of B in the 0–0.2 T range (red solid curve in figure 4(a)). This gives $\tau_\varphi = 31.95$ ps, $\tau_i = 33.2$ ps and $\tau_* = 0.29$ ps. Thus, we are in the condition $\tau_* \ll \tau_{\varphi,i}$, where the zero-field antilocalization term δ_0 is suppressed to the point of being negligible [58, 59].

We can compare these results with the existing literature at $T = 4$ K, immediately before the signal saturation for $T \lesssim 4$ K, shown in figure 4(b). Ref. [67] presented a WL study in SLG for different carrier densities, expressed in terms of the characteristic length-scales $L_{\varphi,i,*} = (D_{\rm tr}\tau_{\varphi,i,*})^{1/2}$. For $n_{2d} \simeq 1.5\cdot 10^{12}$ cm^{-2} and $T = 4$ K, they report $L_\varphi = 1.5$ μm, $L_i = 0.8$ μm and $L_* = 75$ nm. This is the value of n_{2d} closest to that in our devices, even if still at least one order of magnitude smaller. The characteristic lifetimes in our device give $L_\varphi = 0.93$ μm, $L_i = 0.95$ μm and $L_* = 88$ nm, in agreement with the existing data [67].

Since the T dependence of τ_φ contains information on the most relevant inelastic scattering mechanisms [49, 57] and following the previous results, we can use equation (1) with $\delta_0 = 0$ to describe the low-T ($\lesssim$20–30 K) part of the R_S as a function of T curves in figure 2. This approach is sound, since the smallest doping in our measurements is $\sim 1\cdot 10^{13}$ cm^{-2}, a large value for solid-dielectric gating experiments [7, 8], and we do not find anti-localized behavior at these doping levels. Refs. [66, 67, 80] also reported that doping strongly enhances τ_*^{-1} (thus reducing δ_0), since trigonal warping becomes more relevant the higher the energy separation from the Dirac point. This makes our approximation $\delta_0 = 0$ valid also for higher doping.

We can thus write the complete expression for the conductance of our FLG devices, valid for $T \lesssim 90$ K:

$$\sigma_{2d} = \sigma_{\rm Drude} + \delta\sigma_{\rm WL} \quad (3)$$

where $\sigma_{\rm Drude}$ is [71]:

$$\sigma_{\rm Drude} = \frac{e^2}{4}\tau\sum_i(\nu_{k_i}\nu_s v_{{\rm F}_i}^2 N_i) = e^2\tau P(n_{2d}) \quad (4)$$

Here ν_{k_i} and ν_s are the valley and spin degeneracies, respectively, $v_{{\rm F}_i}$ is the Fermi velocity and N_i the DOS at the $E_{\rm F}$ of the ith band. Taking into account the Matthiessen rule [101] on the carrier lifetime at finite T we have:

$$\tau^{-1} = \tau_{\rm tr}^{-1} + \tau_{\rm inel}^{-1} \quad (5)$$

where $\tau_{\rm inel}$ is the T-dependent inelastic scattering lifetime. Substituting in equation (3) we get:

$$\sigma_{2d} = e^2P(n_{2d})\cdot\left(\tau_{\rm tr}^{-1} + \tau_{\rm inel}^{-1}\right)^{-1} - \frac{e^2}{\pi h}\ln\left(1+2\frac{\tau_\varphi}{\tau_i}\right) \quad (6)$$

In order to proceed further, we need to determine the prefactor $P(n_{2d})$, the transport lifetime $\tau_{\rm tr}$ and the T dependence of τ_φ.

We estimate $P(n_{2d})$ by computing the FLG band-structure through *ab initio* Density Functional Theory (DFT) for all our doping levels. We also perform a consistency check of the DFT estimations by running independent self-consistent tight-binding calculations for the doped 4LG. Here we present the results for Bernal stacked 4LG and 5LG. As a first approximation, we assume these systems to be isolated, i.e. we consider the effects of the substrate to be negligible.

We first investigate the band-structures of FLG within the all-electron, full-potential, linear augmented plane wave (FP-LAPW) method as implemented in the ELK code [72]. The local density approximation (LDA)

[73] is used to describe the exchange and correlation. We fix the in-plane lattice constant to a = 2.46 Å, i.e. the experimental in-plane lattice constant of graphite [74]. To model FLG we consider a three-dimensional supercell with a very high value of the c lattice constant so that the periodic images of the structures are at least 10 Å apart, in order to avoid interactions (e.g. for 4LG we take c = 40 a.u.) while the layer-layer distance is taken to be 3.35 Å independent of N. Doping is simulated by adding electrons to the systems, together with a compensating positive background, as in refs. [28, 75] (Jellium model). The Brillouin zone is sampled with a $28 \times 28 \times 1$k-point mesh. The radius of the muffin-tin spheres for the carbon atoms is taken as $1.342a_0$, where a_0 is the Bohr radius. We set $R_{MT}K_{max} = 8$, where R_{MT} is the smallest muffin-tin radius, K_{max} is a cutoff wave vector and the charge density is Fourier expanded up to a maximum wave vector $G_{max} = 12a_0$. The convergence of self-consistent field calculations is attained with a total energy tolerance of 10^{-8} Hartree.

Figure 5 plots the results for both 4LG (panel a) and 5LG (panel b) for different doping. The extra induced charge shifts E_F away from the Dirac point, eventually crossing multiple bands at K and K'. In all cases, the crossing occurs well within regions where the energy dispersion is nearly linear. For the highest V_G (+3 and +4 V), an additional important feature appears in the bandstructure. The large induced charge density brings down a further band at Γ, which becomes populated and can thus contribute to transport. The dispersion of this new band is parabolic, and its appearance is reminiscent of that of the interlayer band induced by alkali metal intercalation in graphite intercalated compounds (GICs) [24].

Our approach neglects the intense electric field at the EDL/graphene interface, that in transition-metal dichalcogenides increases with doping and affects the effective mass value [40]. The simplified Jellium model was shown to capture the fundamental physics of doped SLG [28] and single-layer MoS_2 [75]. We thus perform a consistency check for 4LG by comparing DFT with tight-binding calculations where the screening of the electric field by the charge carriers is accounted for. We compare the same terms $\sum_i \nu_{F_i}^2 N_i$. The ν_{F_i} and N_i values obtained by tight-binding and DFT are within 30%. This suggests that our DFT approach is correct at least to a first-order approximation.

These calculations allow us to obtain both the DOS and the electron velocity of the populated bands at E_F which, in turn, according to equation (4), determine $P(n_{2d})$. Once $P(n_{2d})$ is known, τ_{tr} can be evaluated. Figure 4(b) shows that, in the absence of WL, the resistance saturates to a constant value for $T \lesssim 8$ K. Thus, the saturation Boltzmann conductance $e^2\tau_{tr}P(n_{2d})$ can be estimated from the minimum R_{SMin} before the onset of the logarithmic upturn. This underestimates the saturation conductance (thus the scattering time) by less than 1%, which is negligible compared to the other sources of uncertainty in the evaluation of τ_{tr}. This approach allows us to compute $\tau_{tr} = 2\tau_e$ as a function of n_{2d} in all our devices as:

$$\tau_{tr}(n_{2d}) = \frac{R_{SMin}^{-1}(n_{2d})}{e^2 P(n_{2d})} \quad (7)$$

3.2. Scattering lifetimes versus temperature

We now consider the T dependence of τ_φ. This can be done by using equation (1) without the δ_0 contribution (since $\tau_* \ll \tau_{\varphi,i}$) in the analysis of the low-T part ($4 < T < 20$ K) of the curves of figure 2. By inverting this simplified expression, we obtain the T dependence of $\tau_\varphi(T)/\tau_i$, as shown in figures 6(a) (4LG) and (b) (5LG). Since τ_i, for $T \lesssim 30$ K, can be assumed almost independent of T [67], the T dependence of τ_φ/τ_i is the same as that of τ_φ. By expressing $\tau_\varphi \propto T^{-p}$, we associate the p value to specific scattering processes. For T lower than the Bloch–Grüneisen T [19], e–ph scattering gives $p = 3$ for a standard 2-dimensional electron gas (2DEG) [53] and $p = 4$ for SLG [19]. The e–e scattering gives $p = 1$ for the Nyquist (small momentum exchange) process [55] and $p = 2$ for the Coulomb (large momentum exchange) process [54]. As shown in figure 6, the τ_φ/τ_i curves show almost no superlinear behavior in the WL region. Nyquist e–e scattering is thus the dominant mechanism in this T range. This is consistent with the existing literature on SLG [66] and 2LG [68, 70]. In ref. [23] we reported that the T dependence below 100 K has a linear plus a quadratic contribution, the linear being dominant for $T_{Min} \lesssim T \lesssim 30$ K (see figures 4(a) and 5(c) of ref. [23]) and assigned this to competing Coulomb and Nyquist e–e scattering processes. This is consistent with the present observation of a dominant Nyquist contribution for $T < 20$ K.

As any energy exchange with the surrounding environment breaks phase coherence [49], WL is suppressed by an increased probability of inelastic scattering associated with the T increase [46]. Thus, since the most relevant contribution to the phase-breaking time τ_φ arises from the inelastic scattering due to e–e interaction $\tau_{inel}|_{e-e}$ [49], we can write the T dependence of τ_φ in the entire 4–90 K range as:

$$\tau_\varphi^{-1} \simeq \tau_{inel}^{-1}|_{e-e} = A \cdot T + B \cdot T^2 \quad (8)$$

By inserting equation (8) in the first terms of the Drude conductance of equation (6), we can fit the curves at different doping in the intermediate T region (30–90 K) where the WL contribution can be neglected. With the previously determined values of $P(n_{2d})$ and $\tau_{tr}(n_{2d})$, this fit provides us the parameters $A(n_{2d})$ and $B(n_{2d})$. Finally, combining $\tau_\varphi(T)$ determined here with $\tau_\varphi(T)/\tau_i$ obtained from the low T (4–20 K) region, we can extract $\tau_i(n_{2d})$. Figure 6(b) shows the agreement between a fit based on equation (8) (black dashed lines) and the experimental data in the WL region (solid lines).

We first apply this procedure to the R_S as a function of T curves of the device on which the magnetoresistance was measured, obtaining $\tau_\varphi = 39.7$ ps and

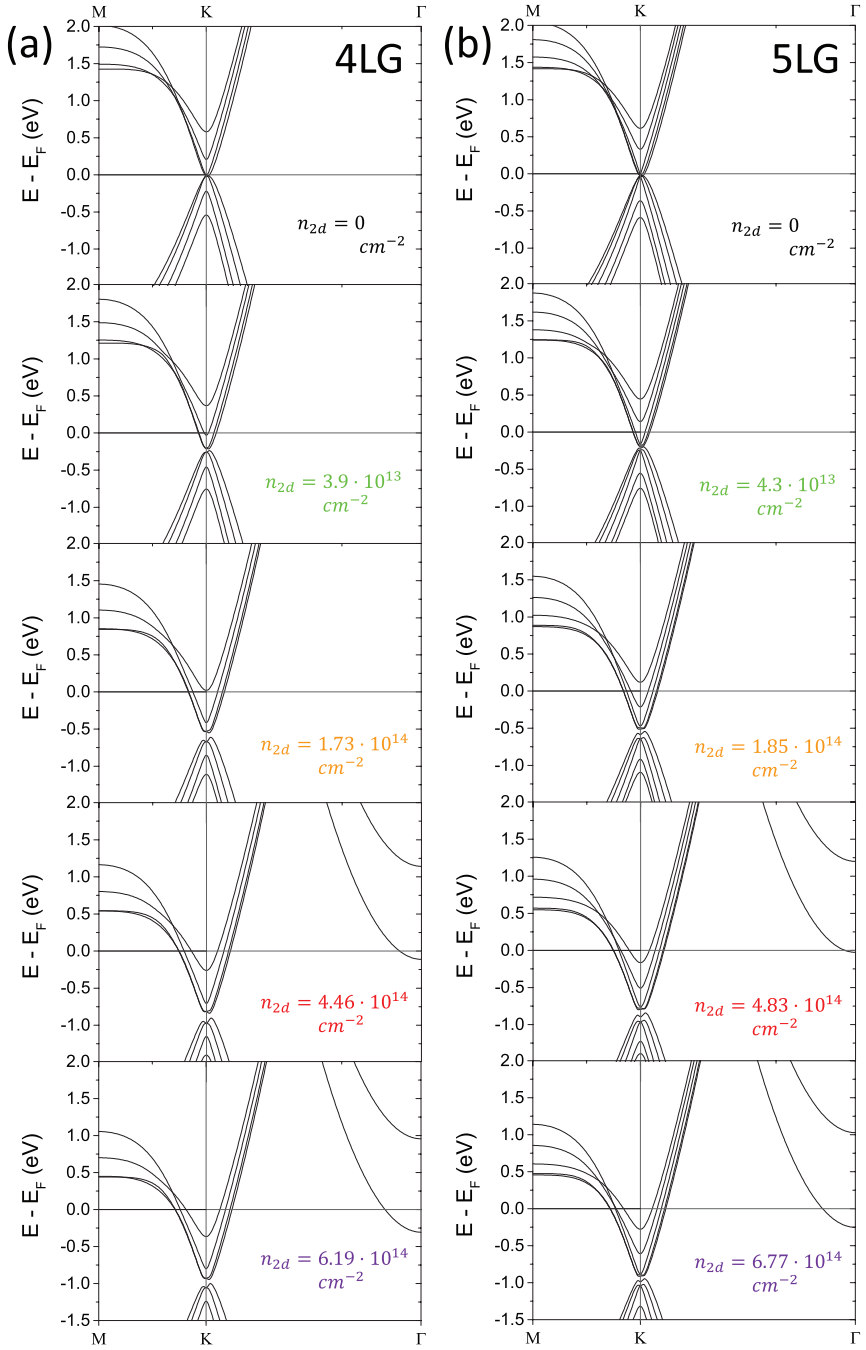

Figure 5. Band structure evolution with increase of doping in 4LG (a) and 5LG (b), for selected values of n_{2d}. For $n_{2d} \lesssim 2 \cdot 10^{14}$ cm^{-2}, the effect of the extra carriers is comparable to a rigid-band shift. Larger doping induces new structures.

$\tau_i = 49.7$ ps at 4 K, in agreement with the values coming from the magnetoresistance fit at 2 K. Once again, the comparison is carried out at 4 instead of 2 K due to the signal saturation for T$\lesssim$4K in figure 4(b). This comparison indicates that the analysis of the magnetoconductance and of the T-dependence of R_S leads to equivalent estimates for τ_φ and τ_i. Thus, since we can perform the R_S versus T characterization of our devices more easily and more extensively than the magnetotransport measurements, due to the thermal expansion coefficient mismatch between the devices and the frozen electrolyte, we repeat the R_S versus T analysis on the 4LG and 5LG devices for different V_G.

3.3. Transport scattering lifetime versus carrier density

We now discuss the measured trends of τ_{tr} as a function of n_{2d}. In standard 2DEGs, such as GaAs heterostructures [43], τ_{tr} is equivalent to the elastic scattering lifetime ($\tau_{tr} = \tau_e$) and follows a n_{2d} dependence, $1 < \gamma < 2$ [43, 94, 95]. This implies that τ_{tr} increases for increasing n_{2d} due to the increased

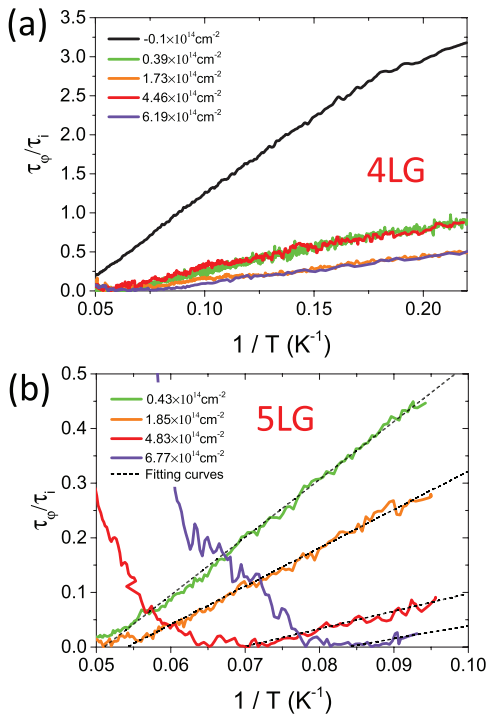

Figure 6. (a) τ_φ/τ_i as a function of $1/T$ obtained from the low-T data ($4 < T < 20$ K) of figure 2(a) (4LG); (b) The same as in (a) but for the low-T data of figure 2(d) (5LG). Dashed lines are fits to the experiments according to equation (8). Best fits for 4LG are omitted for clarity.

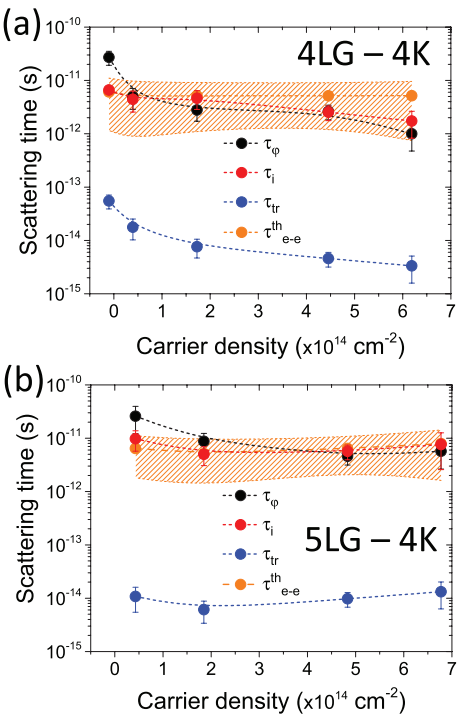

Figure 7. (a) n_{2d} dependence of τ_φ (black dots), τ_i (red dots), τ_{tr} (blue dots) and $\tau_\varphi|^{th}_{e\text{-}e}$ (orange dots and shaded band) at 4 K in 4LG; (d) The same as in (a) but for 5LG. Dashed lines act as guides to the eye.

screening of elastic scatterers by the increased density of charge carriers [86, 87]. In our devices, however, τ_{tr} does not follow this behavior, suggesting a significant increase of the number of elastic scatterers with increasing gate voltage.

If we consider the 4LG device first, we observe that τ_{tr} shows a monotonically decreasing behavior (figure 7(a), blue dots). One possible explanation was suggested in ref. [88], where the authors reported a decreasing mobility at high n_{2d} for 2DEGs. In contrast to Coulomb disorder, short-range disorder would become stronger with increasing n_{2d}, thus increasing the scattering rate [88]. However, we think that this is not the main source of the increase of τ_{tr} in our case. A degradation of the mobility of EDL-gated devices was reported in strontium titanate [76] and rhenium disulfide [77], where it was suggested that ions in the electrolyte act as charged impurities. Thus, we attribute this effect to the microscopic dynamics of how EDL gating induces extra carriers. EDL gating is able to induce modulations in excess of 10^{14} cm^{-2} to n_{2d} by accumulating a packed layer of ions in close proximity (~1 nm [7, 8]) to its surface. Refs. [78, 79] reported that charge-donating impurities at the SLG surface act as scattering centers.

We thus propose that the Li^+ ions in the EDL have a similar role. Their increased density with V_G competes with the increased screening induced by the extra carriers and this determines τ_{tr}. In 4LG, the former effect would be stronger in the entire n_{2d} range, resulting in the monotonic reduction of τ_{tr}. If this is the case, we expect 5LG to be less sensitive to the extra scattering centers. These are localized at the surface of the first layer, and ref. [76] showed that introducing a thin spacer between the ions and the conductive channel greatly improves carrier mobility. With respect to 4LG, 5LG features one further conductive channel due to the fifth layer, which is thus further separated from the scattering centers. Indeed, this is what we observe: the 5LG device shows an initial decrease for $n_{2d} \lesssim 2 \cdot 10^{14}$ cm^{-2} followed by an increase for $n_{2d} \gtrsim 4 \cdot 10^{14}$ cm^{-2} (figure 7(b), blue dots). Overall, the τ_{tr} in 5LG is nearly constant with n_{2d}, as if the two competing effects on mobility were almost canceling out. As for 3LG, we estimate $\tau_{tr} \sim 2.5$ fs at $n_{2d} \sim 5.2 \cdot 10^{14}$ cm^{-2}, which is smaller than in 4LG. This corresponds to a suppression by a factor ~18 of the low-n_{2d} value in 3LG, higher than the ~15 times one in 4LG. Thus, 3LG appears even more sensitive to the accumulation of scattering centers at its surface than 4LG, in accordance with the previous results.

3.4. Dephasing and intervalley scattering lifetimes versus carrier density

Let us now consider the doping dependence of τ_φ and τ_i in 4LG and 5LG, in order to allow for a direct comparison with the corresponding values for 3LG estimated from magnetoresistance. Figure 7 shows that the doping dependence of τ_i is weakly decreasing or nearly constant within the uncertainty range: from 6.6 ± 0.7 ps to 1.7 ± 0.9 ps for 4LG, from 9.8 ± 4.1 ps to 7.6 ± 5.0 ps for

5LG. This dependence was already observed [66, 80], albeit for $n_{2d} \lesssim 1.5 \cdot 10^{13}$ cm^{-2}, much lower than the n_{2d} considered here ($n_{2d} \gtrsim 1 \cdot 10^{14}$ cm^{-2}). In contrast, the doping dependence of τ_φ is more significant, as it is monotonically decreasing in the entire range in 4LG, while it shows a small inversion in slope on the final point for 5LG. These results are in contrast with earlier findings on FLG for $n_{2d} < 2 \cdot 10^{13}$ cm^{-2} [80]. As already pointed out, e–e Nyquist scattering is the dominant dephasing mechanism in the low T range. Therefore, we can write [43]:

$$\tau_\varphi^{-1}|_{e\text{-}e}(T) = \frac{k_B T}{2\hbar}\frac{\ln(x)}{x}, \qquad x = \frac{E_F \tau_e}{\hbar}. \quad (9)$$

The condition $x \sim 1$ (Ioffe–Regel criterion [96]) characterizes the Anderson metal-to-insulator transition [97]. The metallic regime corresponds to $x \gg 1$, leading to a τ_φ increasing with n_{2d} (i.e. with increasing E_F). Under strong localization conditions, $x < 1$ and the Boltzmann model no longer holds [98]. Intermediate x values mark a crossover from strong to weak localization [99] and correspond to a region where τ_φ can exhibit a decreasing behavior with n_{2d}. The exact form of the $\tau_\varphi(n_{2d})$ curves is determined by the dependence of E_F on n_{2d} (which, in the linear regions of the bands, is a square root [100]) and on τ_e. If we compute the value of x corresponding to our data by using the τ_φ values determined at 4 K, we find that, for 4LG, $x = 2.7 \pm 0.2$ in the entire range of negative charge induction, while, for 5LG, $x < 2.7$ for $V_G = 1$ and 2 V, $x > 5$ for $V_G = 3$ and 4 V. Thus, the 4LG device is always in the 'crossover' condition, while in 5LG the typical 2DEG behavior is restored for $n_{2d} \gtrsim 2 \cdot 10^{14}$ cm^{-2}. Due to the dependence of x on τ_e, these results are consistent with the fact that the ion dynamics in the EDL gating provides a competition between an increase of the number of elastic scattering centers and of n_{2d} with increasing V_G. In 4LG the concurrent increase of E_F and decrease of $\tau_{tr} = 2\tau_e$ (see figure 7(a)) could maintain x almost constant. In 5LG at $n_{2d} \gtrsim 2 \cdot 10^{14}$ cm^{-2} the increase of both E_F and τ_{tr} (see figure 7(b)) would eventually lead to the increase of x. This behavior could be due to the differences in both surface-to-volume ratio and bandstructure of 4LG and 5LG, and is in agreement with the behavior of τ_{tr} in the two samples.

3.5. Comparison with the single-band scattering model

In order to further analyze these results, we evaluate the theoretical values of the e–e scattering lifetimes by using the definition of x given in equation (9) with $E_F(n_{2d})$ determined by DFT and τ_e taken from the determined τ_{tr} values. The results are shown in figure 7 as orange circles and shaded bands (that represent the uncertainty regions). Our τ_φ (black dots) are in agreement with the theoretical predictions within an order-of-magnitude. However, the latter are nearly doping-independent in contrast with experiments. This different behavior is particularly evident in 4LG. As expected, the addition of the Coulomb scattering term [66] does not affect appreciably the predicted values at this low T. Since the theoretical $\tau_{e\text{-}e}$ are dependent on the details of the *ab initio* calculations, the inconsistency might be related to the approximations in the DFT calculations of the effects of the high electric field. However, a more important reason for the mismatch lies in the limitation of the hypotheses underlying the theoretical derivation of the Nyquist scattering. Both the single-band and the parabolic-dispersion assumptions do not hold in FLG, particularly when the E_F is so far from the Dirac point [92, 93].

3.6. Comparison with the scattering lifetimes as determined by pump-probe spectroscopy

A comparison with the other experimental technique able to probe the e–e scattering lifetime, i.e. pump-probe spectroscopy, is not immediate, due to the different conditions in the probed electron system between transport and spectroscopic measurements. Low-bias (<0.2 V [105]) transport measurements, such as the ones in this work, involve only scattering processes between carriers very close to the E_F. Pump-probe measurements, on the other hand, generate a strongly out-of-equilibrium carrier population by optical excitation. This population first thermalizes to a quasi-equilibrium distribution of 'hot' carriers via e–e [106, 108, 111] and e–ph [105–110] scattering processes. The 'hot' carriers then cool down to the rest of the Fermi sea over a much longer time scale by scattering with optical phonons [105–111]. This makes the two types of measurements hardly comparable, as the e–e scattering lifetime is heavily dependent on the difference in energy between the scattering electrons and the E_F [104, 112]. Moreover, pump-probe experiments are typically performed at room T [106–108, 110, 111], where the Coulomb term dominates e–e scattering, while our experiments are at low T, where the Nyquist term dominates. With all these caveats, if we extrapolate to room T the e–e scattering lifetimes using equation (9) and imposing $T = 300$ K. This gives $\tau_{e\text{-}e}$ between ~1 and 7 fs, in agreement with existing literature [106, 108, 111].

4. Conclusions

We explored the electronic transport properties of 3-, 4- and 5-layer graphene in the doping regime in excess of $\sim 10^{13}$–10^{14} cm^{-2} and in the 4–30 K temperature range. We used electric double layer gating to dope the samples up to $\sim 7 \cdot 10^{14}$ cm^{-2}. We found evidence of quantum coherent transport in the entire carrier density range. Magnetoresistance measurements showed that, in the 4–30 K range, transport is dominated by weak localization in the diffusive regime, and that the behavior of 3LG, 4LG and 5LG is described by the theoretical models developed for SLG and 2LG. We combined the experimental results with DFT calculations to determine the carrier scattering lifetimes as a function of the carrier density for different number of layers, and determined

that electron–electron scattering with small momentum transfer (Nyquist process) is the main source of dephasing at low temperatures. Both the transport scattering lifetime and the phase coherence lifetime show a non-trivial dependence on n_{2d}. We explained the behavior of τ_{tr} in terms of a competing modulation of doping and density of charged scattering centers induced by EDL gating. The doping dependence of τ_{φ} points to a gate-tunable crossover from weak to strong localization, highlighting the limits of applying single-band models to multi-band systems, such as heavily doped few-layer graphene.

Acknowledgments

We thank M Calandra, M Polini and V Brosco for useful discussions. We acknowledge funding from EU Graphene Flagship, ERC Grant Hetero2D, EPSRC Grant Nos. EP/ K01711X/1, EP/K017144/1, EP/ N010345/1, and EP/L016087/1 and the Joint Project for the Internationalization of Research 2015 launched by Politecnico di Torino under funding of Compagnia di San Paolo.

References

[1] Panzer M J, Newman C R and Frisbie C D 2005 Low-voltage operation of a pentacene field-effect transistor with a polymer electrolyte gate dielectric *Appl. Phys. Lett.* **86** 103503
[2] Bayer M, Uhl C and Vogl P 2005 Theoretical study of electrolyte gate AlGaN/GaN field effect transistors *J. Appl. Phys.* **97** 033703
[3] Yuan H T, Shimotani H, Tsukazaki A, Ohtomo A, Kawasaki M and Iwasa Y 2009 High-density carrier accumulation in ZnO field-effect transistors gated by electric double layers of ionic liquids *Adv. Funct. Mater.* **19** 1046–53
[4] Ueno K, Nakamura S, Shimotani H, Ohtomo A, Kimura N, Nojima T, Aoki H, Iwasa Y and Kawasaki M 2008 Electric-field-induced superconductivity in an insulator *Nat. Mater.* **7** 855–8
[5] Ye J T, Inoue S, Kobayashi K, Kasahara Y, Yuan H T, Shimotani H and Iwasa Y 2009 Liquid-gated interface superconductivity on an atomically flat film *Nat. Mater.* **9** 125–8
[6] Ye J T, Zhang Y J, Akashi R, Bahramy M S, Arita R and Iwasa Y 2012 Superconducting dome in a gate-tuned band insulator *Science* **338** 1193
[7] Ueno K, Shimotani H, Yuan H T, Ye J T, Kawasaki M and Iwasa Y 2014 Field-induced superconductivity in electric double layer transistors *J. Phys. Soc. Japan* **83** 032001
[8] Fujimoto T and Awaga K 2013 Electric-double-layer field-effect transistors with ionic liquids 2013 *Phys. Chem. Chem. Phys.* **15** 8983
[9] Goldman A M 2014 Electrostatic gating of ultrathin films *Annu. Rev. Mater. Res.* **44** 45
[10] Saito Y, Nojima T and Iwasa Y 2016 Gate-induced superconductivity in two-dimensional atomic crystals 2016 *Supercond. Sci. Technol.* **29** 093001
[11] Das A *et al* 2008 Monitoring dopants by Raman scattering in an electrochemically top-gated graphene transistor *Nat. Nanotechnol.* **3** 210
[12] Das A, Chakraborty B, Piscanec S, Pisana S, Sood A K and Ferrari A C 2009 Phonon renormalization in doped bilayer graphene *Phys. Rev.* B **79** 155417
[13] Chen F, Qing Q, Xia J L, Li J H and Tao N J 2009 Electrochemical gate-controlled charge transport in graphene in ionic liquid and aqueous solution *J. Am. Chem. Soc.* **131** 9908
[14] Pachoud A, Jaiswal M, Ang P K, Loh K P and Ozyilmaz B 2010 Graphene transport at high carrier densities using a polymer electrolyte gate *Europhys. Lett.* **92** 27001
[15] Efetov D K and Kim P 2010 Controlling electron–phonon interactions in graphene at ultrahigh carrier densities *Phys. Rev. Lett.* **105** 256805
[16] Lui C H, Li Z Q, Mak K F, Cappelluti E and Heinz T F 2011 Observation of an electrically tunable band gap in trilayer graphene *Nat. Phys.* **7** 944
[17] Ye J, Craciun M F, Koshino M, Russo S, Inoue S, Yuan H, Shimotani H, Morpurgo A F and Iwasa Y 2011 Accessing the transport properties of graphene and its multilayers at high carrier density *Proc. Natl. Acad. Sci. USA* **108** 32
[18] Chen Z Y, Yuan H T, Zhang Y F, Nomura K, Gao T, Gao Y, Shimotani H, Liu Z F and Iwasa Y 2012 Tunable spin–orbit interaction in trilayer graphene exemplified in electric-double-layer transistors *Nano Lett.* **12** 2212
[19] Hwang E H and Das Sarma S 2008 Acoustic phonon scattering limited carrier mobility in two-dimensional extrinsic graphene *Phys. Rev.* B **77** 115449
[20] Jo S, Costanzo D, Berger H and Morpurgo A F 2015 Electrostatically induced superconductivity at the surface of WS_2 *Nano Lett.* **15** 1197
[21] Daghero D, Paolucci F, Sola A, Tortello M, Ummarino G A, Agosto M, Gonnelli R S, Nair J R and Gerbaldi C 2012 Large conductance modulation of gold thin films by huge charge injection via electrochemical gating *Phys. Rev. Lett.* **108** 066807
[22] Tortello M, Sola A, Sharda K, Paolucci F, Nair J R, Gerbaldi C, Daghero D and Gonnelli R S 2013 Huge field-effect surface charge injection and conductance modulation in metallic thin films by electrochemical gating *Appl. Surf. Sci.* **269** 17
[23] Gonnelli R S *et al* 2015 Temperature dependence of electric transport in few-layer graphene under large charge doping induced by electrochemical gating *Sci. Rep.* **5** 9554
[24] Profeta G, Calandra M and Mauri F 2012 Phonon-mediated superconductivity in graphene by lithium deposition *Nat. Phys.* **8** 131
[25] Delahaye J J, Lindell R, Sillanp M, Paalanen M, Sepp H and Hakonen P 2003 Low-Noise current amplifier based on Mesoscopic Josephson junction *Science* **299** 1045
[26] De Franceschi S, Kouwenhoven L, Sch C and Wernsdorfer W 2010 Hybrid superconductor quantum dot devices *Nat. Nanotechnol.* **5** 703
[27] Huefner M, May C, Kicin S, Ensslin K, Ihn T, Hilke M, Suter K, de Rooij N F and Staufer U 2009 Scanning gate microscopy measurements on a superconducting single-electron transistor *Phys. Rev.* B **79** 134530
[28] Margine E R and Giustino F 2014 Two-gap superconductivity in heavily n-doped graphene: *ab initio* Migdal-Eliashberg theory *Phys. Rev.* B **90** 014518
[29] Ludbrook B M *et al* 2015 Evidence for superconductivity in Li-decorated monolayer graphene *Proc. Natl Acad. Sci. USA* **112** 11795
[30] Ichinokura S, Sugawara K, Takayama A, Takahashi T and Hasegawa S 2016 Superconducting calcium-intercalated bilayer graphene *ACS Nano* **10** 2761
[31] Bruna M and Borini S 2009 Optical constants of graphene layers in the visible range *Appl. Phys. Lett.* **94** 031901
[32] Novoselov K S, Jiang D, Schedin F, Booth T J, Khotkevich V V, Morozov S V and Geim A K 2005 Two-dimensional atomic crystals *Proc. Natl Acad. Sci. USA* **102** 10451
[33] Bonaccorso F, Lombardo A, Hasan T, Sun Z P, Colombo L and Ferrari A C 2012 Production and processing of graphene and 2d crystals *Mater. Today* **15** 564
[34] Ferrari A C and Basko D 2013 Raman spectroscopy as a versatile tool for studying the properties of graphene *Nat. Nanotechnol.* **8** 235
[35] Ferrari A C *et al* 2006 Raman spectrum of graphene and graphene layers *Phys. Rev. Lett.* **97** 187401
[36] Casiraghi C, Hartschuh A, Lidorikis E, Qian H, Harutyunyan H, Gokus T, Novoselov K S and Ferrari A C 2007 Rayleigh imaging of graphene and graphene layers *Nano Lett.* **7** 2711
[37] Bruna M, Ott A K, Ijas M, Yoon D H, Sassi U and Ferrari A C 2014 Doping dependence of the Raman spectrum of defected graphene *ACS Nano* **8** 7432

[38] Cancado L G *et al* 2011 Quantifying defects in graphene via Raman spectroscopy at different excitation energies *Nano Lett.* **11** 3190

[39] Scholz F and Inzelt G 2010 *Electroanalytical Methods* 2nd edn (Berlin Heidelberg: Springer-Verlag) pp 147–58

[40] Brumme T, Calandra M and Mauri F 2015 First-principles theory of field-effect doping in transition-metal dichalcogenides: structural properties, electronic structure, Hall coefficient, and electrical conductivity *Phys. Rev.* B **91** 155436

[41] Wheeler R G, Choi K K, Goel A, Wisnieff R and Prober D E 1982 Localization and electron–electron interaction effects in submicron-width inversion layers *Phys. Rev. Lett.* **49** 1674

[42] Choi K K, Tsui D C and Palmateer S C 1986 Electron–electron interactions in GaAs/Al_xGa_{1x}As heterostructures *Phys. Rev.* B **33** 8216

[43] Hansen J E, Taboryski R and Lindelhof P E 1993 Weak localization in a GaAs heterostructure close to population of the second subband *Phys. Rev.* B **47** 16040

[44] Sarachik M P, Corenzwit E and Longinotti L D 1964 Resistivity of Mo-Nb and Mo–Re Alloys Containing 1Fe *Phys. Rev.* **135** A1041

[45] Kondo J 1964 Resistance minimum in dilute magnetic alloys *Prog. Theor. Phys.* **32** 37

[46] Bergmann G 1984 Weak localization in thin films: a time-of-flight experiment with conduction electrons *Phys. Rep.* **107** 1
Bergmann G 1983 Physical interpretation of weak localization: a time-of-flight experiment with conduction electrons *Phys. Rev.* B **28** 2914

[47] Larkin A I and Khmelnitsky D E 1982 Anderson localization and anomalous magnetoresistance at low temperatures *Usp. Fiz. Nauk* **136** 536
Larkin A I and Khmelnitsky D E 1982 Anderson localization and anomalous magnetoresistance at low temperatures *Sov. Phys.—Usp.* **25** 185

[48] Chen J H, Li L, Cullen W G, Williams E D and Fuhrer M S 2011 Tunable Kondo effect in graphene with defects *Nat. Phys.* **7** 535–8

[49] Beenakker C W J and van Houten H 1991 Quantum transport in semiconductor nanostructures *Solid State Phys.* **44** 1

[50] Altshuler B L, Aronov A G and Lee P A 1980 Interaction effects in disordered Fermi systems in two dimensions *Phys. Rev. Lett.* **44** 19

[51] Altshuler B L and Aronov A G 1985 *Electron–electron Interactions in Disordered Systems* ed A L Efros and M Pollak (Amsterdam: North-Holland) p 1

[52] Fukuyama H 1985 *Electron–electron Interactions in Disordered Systems* ed A L Efros and M Pollak (Amsterdam: North-Holland) p 155

[53] Taboryski R and Lindelhof P E 1990 Weak localisation and electron–electron interactions in modulation-doped GaAs/AlGaAs heterostructures *Semicond. Sci. Technol.* **5** 933

[54] Narozhny B N, Zala G and Aleiner I L 2002 Interaction corrections at intermediate temperatures: dephasing time *Phys. Rev.* B **65** 180202

[55] Altshuler B L, Aronov A G and Khmelnitsky D E 1982 Effects of electron–electron collisions with small energy transfers on quantum localisation *J. Phys. C: Solid State Phys.* **15** 7367

[56] Altshuler B L, Khmel'nitzkii D, Larkin A I and Lee P A 1980 Magnetoresistance and Hall effect in a disordered two-dimensional electron gas *Phys. Rev.* B **22** 5142

[57] Hikami S, Larkin A I and Nagaoka Y 1980 Spin–orbit interaction and magnetoresistance in the two dimensional random system *Prog. Theor. Phys.* **63** 707

[58] McCann E, Kechedzhi K, Falko V I, Suzuura H, Ando T and Altshuler B L 2006 Weak-localization magnetoresistance and valley symmetry in graphene *Phys. Rev. Lett.* **97** 146805

[59] Fal'ko V I, Kechedzhi K, McCann E, Altshuler B L, Suzuura H and Ando T 2007 Weak localization in graphene *Solid State Commun.* **143** 33

[60] Ando T, Nakanishi T and Saito R 1998 Berry's phase and absence of back scattering in carbon nanotubes *J. Phys. Soc. Japan* **67** 2857

[61] Ando T 2005 Theory of electronic states and transport in carbon nanotubes *J. Phys. Soc. Japan* **74** 777

[62] Zhang Y, Tan Y W, Stormer H L and Kim P 2005 Experimental observation of the quantum Hall effect and Berry's phase in graphene *Nature* **438** 201

[63] Suzuura H and Ando T 2002 Crossover from symplectic to orthogonal class in a two-dimensional honeycomb lattice *Phys. Rev. Lett.* **89** 266603

[64] Suzuura H and Ando T 2003 Anderson localization in a graphene sheet *J. Phys. Soc. Japan* **72** 69

[65] Novoselov K S 2006 Unconventional quantum Hall effect and Berry's phase of 2π in bilayer graphene *Nat. Phys.* **2** 177

[66] Tikhonenko F V, Kozikov A A, Savchenko A K and Gorbachev R V 2009 Transition between electron localization and antilocalization in graphene *Phys. Rev. Lett.* **103** 226801

[67] Tikhonenko F V, Horsell D W, Gorbachev R V and Savchenko A K 2008 Weak localization in graphene flakes *Phys. Rev. Lett.* **100** 056802

[68] Gorbachev R V, Tikhonenko F V, Mayorov A S, Horsell D W and Savchenko A K 2007 Weak localization in bilayer graphene *Phys. Rev. Lett.* **98** 176805

[69] Kozikov A A, Savchenko A K, Narozhny B N and Shytov A V 2010 Electron–electron interactions in the conductivity of graphene *Phys. Rev.* B **82** 075424

[70] Chen Y F, Bae M H, Chialvo C, Dirks T, Bezryadin A and Mason N 2011 Negative and positive magnetoresistance in bilayer graphene: effects of weak localization and charge inhomogeneity *Physica* B **406** 785

[71] Cappelluti E and Benfatto L 2009 Vertex renormalization in dc conductivity of doped chiral graphene *Phys. Rev.* B **79** 035419

[72] http://elk.sourceforge.net

[73] Perdew J P and Zunger A 1981 Self-interaction correction to density-functional approximations for many-electron systems *Phys. Rev.* B **23** 5048

[74] Slonczewski J C and Weiss P R 1958 Band structure of graphite *Phys. Rev.* **109** 272

[75] Ge Y and Liu A 2013 Phonon-mediated superconductivity in electron-doped single-layer MoS 2: a first-principles prediction *Phys. Rev.* B **87** 241408

[76] Gallagher P, Lee M Y, Petach T A, Stanwyck S W, Williams J R, Watanabe K, Taniguchi T and Goldhaber-Gordon D 2015 A high-mobility electronic system at an electrolyte-gated oxide surface *Nat. Commun.* **6** 6437

[77] Ovchinnikov D, Gargiulo F, Allain A, Pasquier D J, Dumcenco D, Ho C H, Yazyev O V and Kis A 2016 Disorder engineering and conductivity dome in ReS_2 with electrolyte gating *Nat. Commun.* **7** 12391

[78] Zhang Y, Brar V W, Girit C, Zettl A and Crommie M F 2009 Origin of spatial charge inhomogeneity in graphene *Nat. Phys.* **5** 722

[79] Strasser C, Ludbrook B M, Levy G, Macdonald A J, Burke S A, Wehling T O, Kern K, Damascelli A and Ast C R 2015 Long- versus short-range scattering in doped epitaxial graphene *Nano Lett.* **15** 2825

[80] Baker A M R *et al* 2012 Weak localization scattering lengths in epitaxial, and CVD graphene *Phys. Rev.* B **86** 235441

[81] Wu X S, Li X B, Song Z M, Berger C and de Heer W A 2007 Weak antilocalization in epitaxial graphene: evidence for chiral electrons *Phys. Rev. Lett.* **98** 136801

[82] Berger C *et al* 2006 Electronic confinement and coherence in patterned epitaxial graphene *Science* **312** 1191

[83] Morozov S V, Novoselov K S, Katsnelson M I, Schedin F, Ponomarenko L A, Jiang D and Geim A K 2006 Strong suppression of weak localization in graphene *Phys. Rev. Lett.* **97** 016801

[84] Ki D K, Jeong D C, Choi J H, Lee H J and Park K S 2008 Inelastic scattering in a monolayer graphene sheet: a weak-localization study *Phys. Rev.* B **78** 125409

[85] Liao Z M, Han B H, Wu H C and Yu D P 2010 Gate voltage dependence of weak localization in bilayer graphene *Appl. Phys. Lett.* **97** 163110

[86] Giuliani G F and Vignale G 2005 *Quantum Theory of the Electron liquid* (Cambridge: Cambridge University Press)
[87] Mahan G D 2000 *Many-Particle Physics* (New York: Kluwer)
[88] Das Sarma S and Hwang E H 2014 Short-range disorder effects on electronic transport in two-dimensional semiconductor structures *Phys. Rev.* B **89** 121413
[89] Liu Y P, Lew W S and Sun L 2011 Enhanced weak localization effect in few-layer graphene *Phys. Chem. Chem. Phys.* **13** 20208
[90] Wang W R, Chen L, Wang Z, Wang Y C, Li T and Wang Y L 2012 Weak localization in few-layer graphene grown on copper foils by chemical vapor deposition *Carbon* **50** 5242
[91] Chuang C S *et al* 2014 Weak localization and universal conductance fluctuations in multi-layer graphene *Curr. Appl. Phys.* **14** 108
[92] Nakamura M and Hirasawa L 2008 Electric transport and magnetic properties in multilayer graphene *Phys. Rev.* B **77** 045429
[93] Koshino M 2010 Interlayer screening effect in graphene multilayers with ABA and ABC stacking *Phys. Rev.* B **81** 125304
[94] Paalanen M A, Tsui D C, Gossard A C and Hwang J C M 1984 Temperature dependence of electron mobility in GaAs/$Al_xGa_{1-x}As$ heterostructures from 1 to 10 K *Phys. Rev.* B **29** 6003
[95] Walukiewicz W, Ruda H E, Lagowski J and Gatos H C 1984 Electron mobility in modulation-doped heterostructures *Phys. Rev.* B **30** 4571
[96] Ioffe A F and Regel A R 1960 Non-crystalline, amorphous and liquid electronic semiconductors *Prog. Semicond.* **4** 237
[97] Mott N F and Davis E A 1979 *Electronic Processes in Noncrystalline Materials* (Oxford: Oxford University Press)
[98] Anderson P W 1958 Absence of diffusion in certain random lattices *Phys. Rev.* **109** 1492
[99] Mott N F 1990 *Metal-Insulator Transitions* (London: Taylor and Francis)
[100] Castro Neto A H, Guinea F, Peres N M R, Novoselov K S and Geim A K 2009 The electronic properties of graphene *Rev. Mod. Phys.* **81** 109
[101] Ashcroft N W and Mermin N D 1976 *Solid State Physics* (London: Thomson Learning)
[102] Rey I, Lass J C, Grondin J and Servant L 1998 Infrared and Raman study of the PEO-LiTFSI polymer electrolyte *Electrochim. Acta* **43** 1505
[103] Chrissopoulou K, Andrikopoulos K S, Fotiadou S, Bollas S, Karageorgaki C, Christofilos D, Voyiatzis G A and Anastasiadis S H 2011 Crystallinity and Chain Conformation in PEO/Layered Silicate Nanocomposites *Macromolecules* **44** 9710
[104] Li Q and Das Sarma S 2013 Finite temperature inelastic mean free path and quasiparticle lifetime in graphene *Phys. Rev.* B **87** 085406
[105] Lazzeri M, Piscanec S, Mauri F, Ferrari A C and Robertson J 2005 Electron Transport and Hot Phonons in Carbon Nanotubes *Phys. Rev. Lett.* **95** 236802
[106] Brida D *et al* 2013 Ultrafast collinear scattering and carrier multiplication in graphene *Nat. Commun.* **4** 1987
[107] Lui C H, Mak K F, Shan J and Heinz T F 2010 Ultrafast Photoluminescence from Graphene *Phys. Rev. Lett.* **105** 127404
[108] Breusing M, Kuehn S, Winzer T, Malic E, Milde F, Severin N, Rabe J P, Ropers C, Knorr A and Elsaesser T 2011 Ultrafast nonequilibrium carrier dynamics in a single graphene layer *Phys. Rev.* B **83** 153410
[109] Sun D, Wu Z K, Divin C, Li X, Berger C, de Heer W A, First P N and Norris T B 2008 Ultrafast relaxation of excited dirac fermions in epitaxial graphene using optical differential transmission spectroscopy *Phys. Rev. Lett.* **101** 157402
[110] Huang L, Hartland G V, Chu L Q, Luxmi L Q, Feenstra R M, Lian C, Tahy K and Xing H 2010 Ultrafast transient absorption microscopy studies of carrier dynamics in epitaxial Graphene *Nano Lett.* **10** 1308
[111] Obraztsov P A, Rybin M G, Tyurnina A V, Garnov S V, Obraztsova E D, Obraztsov A N and Svirko Y P 2011 Broadband light-induced absorbance change in multilayer graphene *Nano Lett.* **11** 1540
[112] Hwang E H, Hu B Y K and Das Sarma S 2007 Inelastic carrier lifetime in graphene *Phys. Rev.* B **76** 115434